Supplementary information

Synthesis of nonstoichiometric pseudobrookite ($Fe_{2-x}Ti_{1+x}O_5$) from ilmenite for use in flexible microsupercapacitors

Yahya Sorkhe[1], Mubashir Mansoor[1], Pegah Bavafa[1], Servet Timur[1], Mustafa Urgen[1], Aytekin Uzunuglu[1], Cuneyt Arslan*[1]

[1] *Metallurgical and Materials Engineering Department, Istanbul Technical University, Istanbul, Turkey*

* Corresponding author: sorkhe20@iru.edu.tr

This Supporting Information provides additional details on precursor composition, thermodynamic considerations, morphological analyses, and graphene characterization used in this study.

1. 1. Composition of the ilmenite

The composition of ilmenite concentrate used as raw material for the synthesis of pseudobrookite is given in table S1.

Table S 1. Composition of ilmenite concentrate.

Component	TiO_2	Fe_2O_3 ^{t}	SiO_2	Al_2O_3	MgO	MnO	CaO	FeO	P_2O_5
Wt. %	44.74	48.59	4.65	0.97	1.31	0.8	1.81	35.5	0.1

1.2. Rietveld refinement of the XRD patterns

The calcined powder X-ray diffraction data were refined by the Rietveld method using Match analysis software as a front-end to FullProf. A Thompson–Cox–Hastings pseudo-Voigt line shape with axial-divergence correction (TCHZ) and an 8-term Chebyshev background were employed. The structural model comprised of Fe-substituted rutile TiO_2 (tetragonal, $P4_2/mnm$), with Fe constrained to substitute on the Ti 2a site (Occ (Ti) = 1 − x, Occ (Fe) = x), and (ii) pseudobrookite Fe_2TiO_5 (orthorhombic, Cmcm) using the conventional setting, with Fe/Ti site constrained across M1 (4c) and M2 (8f) and all oxygen sites were kept fully occupied. A single preferred-orientation parameter (March–Dollase) was tested and only retained if it measurably reduced systematic intensity misfit. The refinement converged smoothly with Rwp = 7.2%, RBragg = 17.9%, and $\chi^2 = 3.4$ (Fig. S 1). The calculated amount for Ti_2FeO_5 (Fe doped Rutile) and Fe_2TiO_5 was approximately 12.7wt% and 87.3 wt.% respectively. We can consider these two phases as a single nonstoichiometric $Fe_{2-x}Ti_{1+x}O_5$ phase. The residuals are featureless and no additional Bragg peaks are observed, indicating no crystalline impurities above the XRD detection limit i.e. ~ (2–3) wt.% under our counting statistics.

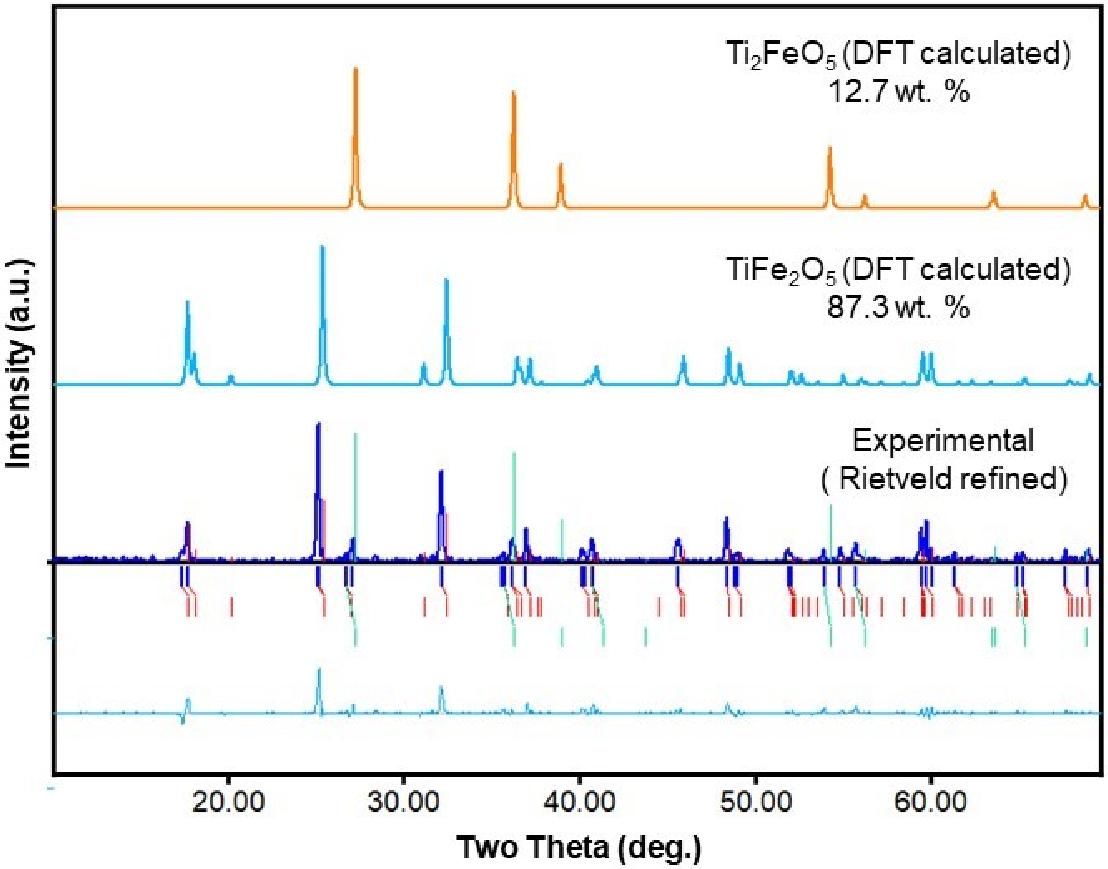

Figure S1. Rietveld refinement of the powder XRD pattern of the pseudobrookite sample.

1.3. Capacitive vs. Diffusive Contribution Analysis (Dunn's Method)

To distinguish between capacitive (surface-controlled) and diffusion limited charge storage, the current response at a fixed potential was analyzed using Dunn's method.[1,2] The total current i(V) in a CV curve can be expressed as:

$$i(V)=K_1\nu+K_2\nu^{1/2} \qquad \text{(S1)}$$

where ν is the scan rate, $K_1\nu$ represents the capacitive contribution, and $K_2\nu^{1/2}$ represents the diffusion-controlled contribution.

Rearranging gives:

$$\frac{i(V)}{\nu^{1/2}}= K_1\nu^{1/2}+K_2 \qquad \text{(S2)}$$

which gives us a linear relationship between $i(V)/\nu^{1/2}$ and $\nu^{1/2}$. From the slope (K_1) and intercept (K_2), the capacitive and diffusion contribution can be quantified at each potential. The capacitive fraction at a given scan rate is obtained from Eq S3 while the remainder corresponds to the diffusion-controlled fraction.

$$\text{Capacitive fraction}=\frac{\int K_1 v dV}{\int i(V) dV} \qquad \text{(S3)}$$

1. 4. Thermodynamic calculation

In the initial step, ilmenite reacts with concentrated sulfuric acid, as shown in reaction 2, producing iron sulfate and titaniumoxysulfate as a porous cake. Subsequently, during the leaching step, both sulfate compounds dissolve in dilute sulfuric acid, resulting in the dissolution of Ti^{4+} and Fe^{2+} as soluble ions. This process is similar to the initial steps of the sulfate process commonly employed for the production of titanium dioxide.[3,4]

$$FeTiO_3 + 2H_2SO_4 \rightarrow FeSO_4 + TiOSO_4 + 2H_2O \qquad \text{(S4)}$$

At the precipitation step Iron sulfate and Titanium oxysulfate reacted with NaOH according:

$$FeSO_4+2NaOH\rightarrow Fe(OH)_2+Na_2SO_4 \qquad \text{(S5)}$$
$$Fe_2(SO_4)_3(aq)+6NaOH(aq)\rightarrow 2Fe(OH)_3(s)+3Na_2SO_4(aq) \qquad \text{(S6)}$$
$$TiOSO_4+2\ NaOH+H_2O\rightarrow Ti(OH)_4+Na_2SO_4 \qquad \text{(S7)}$$

and during the calcination step:

$$2Fe\ (OH)_3 + Ti\ (OH)_4 \rightarrow Fe_2TiO_5 + 5H_2O \qquad \text{(S8)}$$
$$2\ Fe\ (OH)_2 + Ti\ (OH)_4 \rightarrow Fe_2TiO_5 + 3\ H_2O \qquad \text{(S9)}$$

The reactions 3, 4 represent a simplified view of the precipitation process. In reality, the chemistry of titanium and iron in aqueous solutions is quite complex, with multiple species and equilibria involved. The formation of hydroxides is a likely intermediate step, but not necessarily the final stable species under all conditions. The Eh-pH diagrams provide a more comprehensive picture of the stable species. In the Eh-pH diagram shown in Figures S1[5–8], the stable species at the 6 to 8 pH range are mainly Fe_2O_3 and TiO_2 but there may be some other phases like K_2SO_4, $FeSO_4$, Fe_2TiO_5, $FeTi_2O_5$, $FeTiO_3$ (which are insoluble) depending on the Eh of the system. For the Fe-Ti-Na-S system the similar phases can be formed at the pH 6-8. The main differences for this case are the formation of $Na_3(FeSO_4)_3$, $Na_6(FeSO_4)_4$ complex (double) salt at this pH range, while there are no complex salts formed for the Fe-Ti-K-S system in this region. The formation of $FeSO_4$, $Na_3(FeSO_4)_3$, $Na_6(FeSO_4)_4$ which can change the stoichiometry of the precipitated Fe atoms and cause the variation in the final Fe/Ti ratio in the pseudobrookite phase. Therefore, controlling the

Eh-pH in the regions which are marked with 3 in both graphs can help to ensure that the whole dissolved Fe and Ti ions will precipitate.

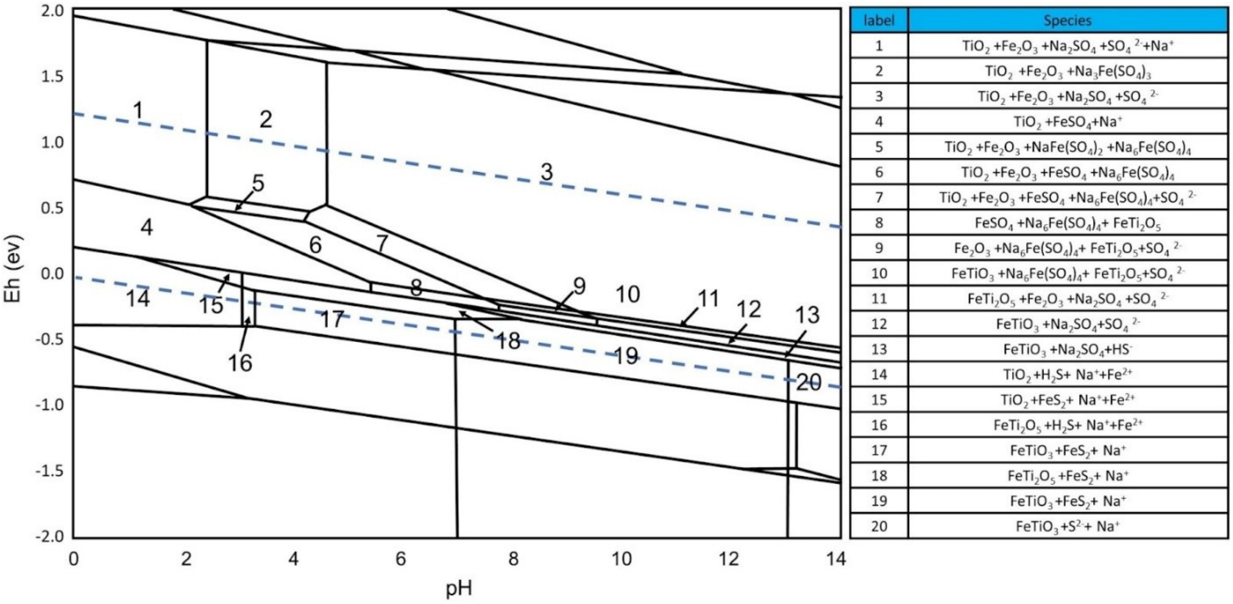

label	Species
1	$TiO_2 + Fe_2O_3 + Na_2SO_4 + SO_4^{2-} + Na^+$
2	$TiO_2 + Fe_2O_3 + Na_3Fe(SO_4)_3$
3	$TiO_2 + Fe_2O_3 + Na_2SO_4 + SO_4^{2-}$
4	$TiO_2 + FeSO_4 + Na^+$
5	$TiO_2 + Fe_2O_3 + NaFe(SO_4)_2 + Na_6Fe(SO_4)_4$
6	$TiO_2 + Fe_2O_3 + FeSO_4 + Na_6Fe(SO_4)_4$
7	$TiO_2 + Fe_2O_3 + FeSO_4 + Na_6Fe(SO_4)_4 + SO_4^{2-}$
8	$FeSO_4 + Na_6Fe(SO_4)_4 + FeTi_2O_5$
9	$Fe_2O_3 + Na_6Fe(SO_4)_4 + FeTi_2O_5 + SO_4^{2-}$
10	$FeTiO_3 + Na_6Fe(SO_4)_4 + FeTi_2O_5 + SO_4^{2-}$
11	$FeTi_2O_5 + Fe_2O_3 + Na_2SO_4 + SO_4^{2-}$
12	$FeTiO_3 + Na_2SO_4 + SO_4^{2-}$
13	$FeTiO_3 + Na_2SO_4 + HS^-$
14	$TiO_2 + H_2S + Na^+ + Fe^{2+}$
15	$TiO_2 + FeS_2 + Na^+ + Fe^{2+}$
16	$FeTi_2O_5 + H_2S + Na^+ + Fe^{2+}$
17	$FeTiO_3 + FeS_2 + Na^+$
18	$FeTi_2O_5 + FeS_2 + Na^+$
19	$FeTiO_3 + FeS_2 + Na^+$
20	$FeTiO_3 + S^{2-} + Na^+$

Figure S2. Eh-pH diagram of Fe-Ti-Na-S system.

1.5. Morphological and elemental characterization of precipitated powder

The SEM and EDS mapping analyses of the as precipitated samples with NaOH shown in Figure S3 displays a highly porous and agglomerated structure characterized by irregular, rough particles. This porous and irregular morphology suggests that NaOH precipitation promotes the formation of amorphous aggregates, as corroborated by the XRD results, likely due to rapid nucleation and growth during the precipitation process.[9,10] Such rapid kinetics can lead to less controlled particle assembly, resulting in the observed agglomeration. EDS mapping further indicates the presence of residual Na_2SO_4 salt which could be due to the inefficient washing during the filtration process. The maps show that Na_2SO_4 is not homogeneously distributed but is instead locally crystallized in specific regions. This localization likely results from the filtration step, where some Na_2SO_4 remains trapped between the precipitated particles during washing. Upon drying, this residual salt solidifies into crystalline Na_2SO_4.[11] The co-localization of sodium (Na) and sulfur (S) in the same regions, as observed in the EDS maps, confirms the presence of Na_2SO_4.

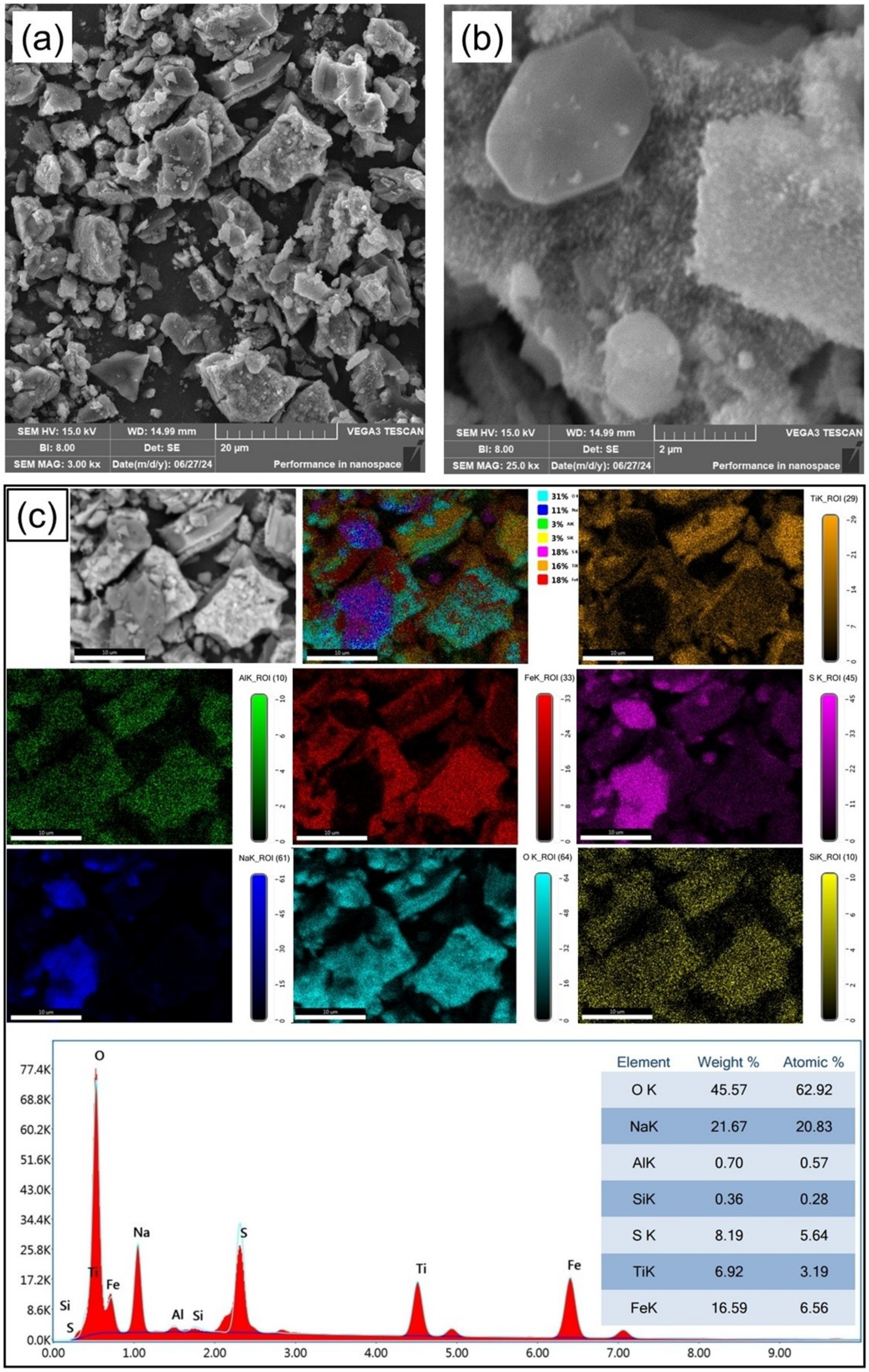

Element	Weight %	Atomic %
O K	45.57	62.92
NaK	21.67	20.83
AlK	0.70	0.57
SiK	0.36	0.28
S K	8.19	5.64
TiK	6.92	3.19
FeK	16.59	6.56

Figure S3. SEM image (a & b) and MAP and EDS analysis of precipitated powder using NaOH before calcination.

1.6. Characterization of graphene

Graphene was prepared by a modified Hummers method, starting from natural graphite powder through oxidative exfoliation to obtain graphene oxide (GO), followed by chemical reduction to yield graphene.[12,13] The structural and morphological features were confirmed by XRD, Raman spectroscopy, SEM, and TEM (Figure S3(a)). The XRD pattern (Figure S4(a)) shows a broad peak centered at 2θ ≈ 26°, corresponding to the (002) plane of graphitic carbon, consistent with few-layer graphene.[14] Raman spectra (Figure S3(b)) display the D band (~1350 cm^{-1}), G band (~1580 cm^{-1}), and a weak 2D band, with an I_D/I_G ratio indicative of defect rich and few layer sheets.[15,16] SEM images (Figure S3(c)) reveal wrinkled, sheet like morphologies with high surface roughness, while STEM (Figure S3(d)) confirms ultrathin nanosheets with lateral sizes in the submicron to micron range, confirming few layers character of synthesized graphene.[17]

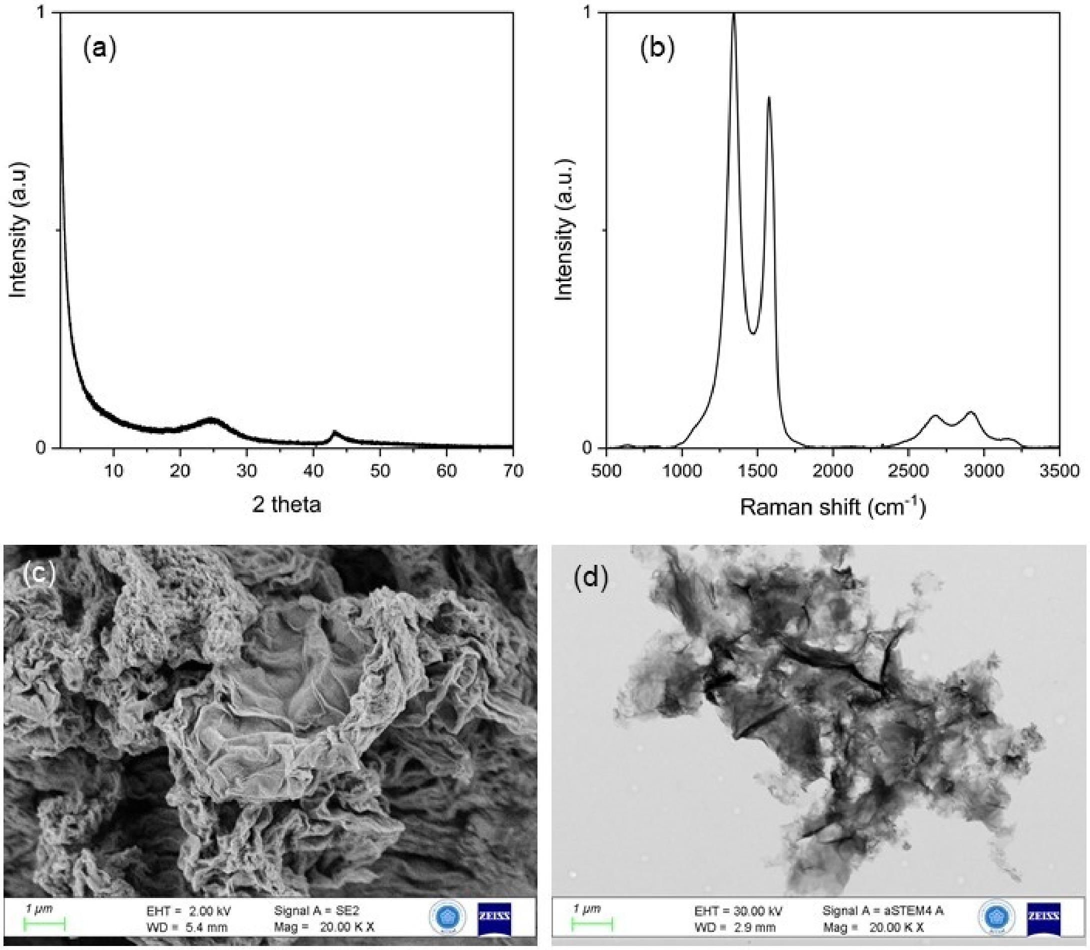

Figure S4. Structural and morphological characterization of graphene synthesized by a modified Hummers method. (a) XRD pattern showing a broad diffraction peak at ~26°(b) Raman spectrum exhibiting characteristic D (~1350 cm^{-1}), G (~1580 cm^{-1}). (c) SEM image revealing wrinkled, sheet-like morphology with high surface roughness. (d) STEM image confirming the ultrathin, transparent nanosheet structure with lateral sizes in the submicron to micron range.

1.7 electrode dimensions and thickness

Figure S5a shows interdigitated pattern with four fingers in each side which each finger has a width of 1.8 mm and spacing, ensuring symmetric current distribution and minimal series resistance across the electrode area. The profilometry analysis after spray coating for three different samples (Figure S5b) reveals that the pseudobrookite films exhibit a approximate thickness of 16 µm over the deposited regions for all three tested samples. The sharp height transition between the PET substrate and the active layer confirms good edge definition after spray-coating and mask removal. Minor variations in height among different scanning lines originate from the surface roughness of the pseudobrookite coating and localized agglomeration of particles during solvent evaporation. The overall uniformity indicates homogeneous deposition and good reproducibility of the fabrication process, which is essential for achieving balanced ion transport and electrochemical performance between interdigitated fingers.

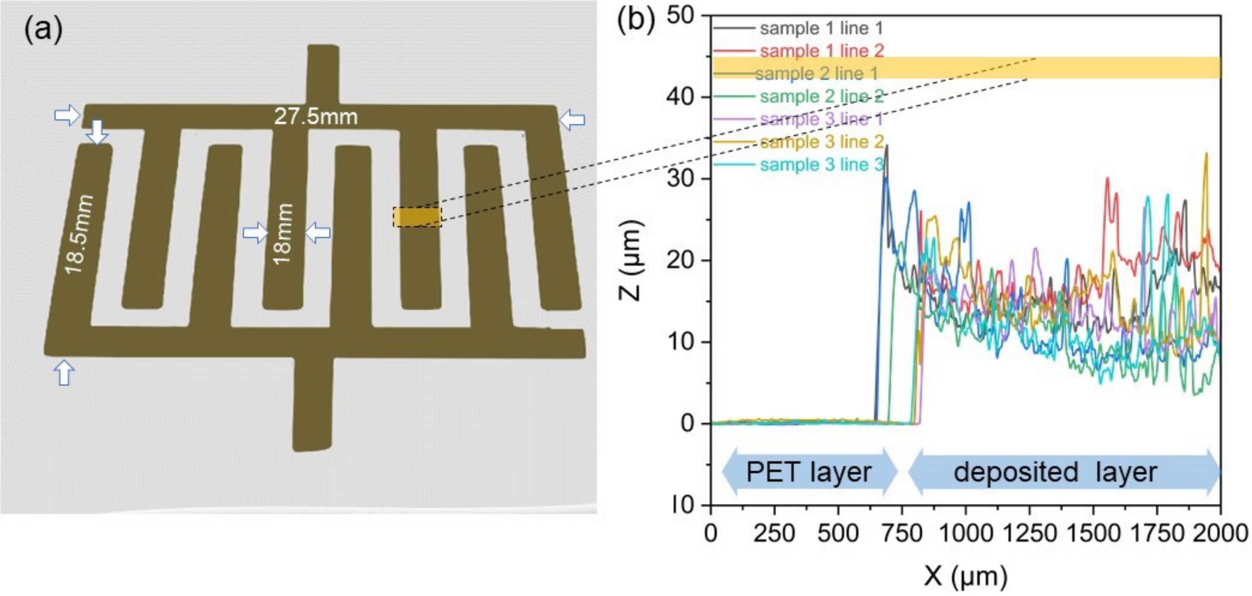

Figure S5. MSC pattern and regarding dimensions (a) and profilometry results of different sample after spray coatings (b).

2. Electrochemical evaluation with bode plot

Electrochemical impedance spectroscopy (EIS) was further analyzed in the form of Bode plots for both symmetric and asymmetric devices (Figure S6). For the symmetric MSC, the impedance magnitude |Z| remains very high at low frequency (~125 kΩ at 0.01 Hz), accompanied by a maximum phase angle of ~70°. This behavior indicates significant internal resistance and only partial capacitive character, consistent with the distorted CV shapes.[18] In contrast, the asymmetric pseudobrookite/graphene MSC displays a much lower impedance magnitude (~6.5 kΩ at 0.01 Hz) and a maximum phase angle of ~38°, confirming improved electronic conductivity and faster ion transport within the hybrid electrode–electrolyte system. The reduced |Z| values in the asymmetric configuration agree well with its superior CV and GCD response, as well as the higher areal energy density reported in the main text.[19,20] These results reinforce the hybrid charge-storage mechanism, where pseudobrookite contributes Faradaic redox pseudocapacitance while graphene and carbon provide rapid double-layer charge storage and electron conduction pathways.

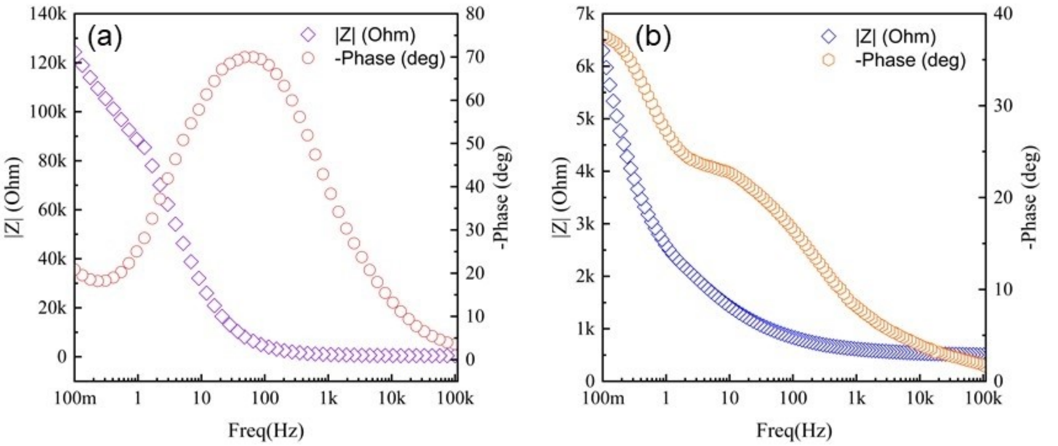

Figure S6. Bode plots of the (a) symmetric pseudobrookite MSC and (b) asymmetric pseudobrookite/graphene MSC.

SI references

1 B. Dunn, H. Kamath and J.-M. Tarascon, *Science*, 2011, **334**, 928–935.
2 V. Augustyn, P. Simon and B. Dunn, *Energy Environ. Sci.*, 2014, **7**, 1597–1614.
3 K. N. Han, T. Rubcumintara and M. C. Fuerstenau, *Metall. Trans. B*, 1987, **18**, 325–330.
4 B. Liang, C. Li, C. Zhang and Y. Zhang, *Hydrometallurgy*, 2005, **76**, 173–179.
5 A. Jain, S. P. Ong, G. Hautier, W. Chen, W. D. Richards, S. Dacek, S. Cholia, D. Gunter, D. Skinner, G. Ceder and K. A. Persson, *APL Mater.*, 2013, **1**, 011002.
6 A. M. Patel, J. K. Nørskov, K. A. Persson and J. H. Montoya, *Phys. Chem. Chem. Phys.*, 2019, **21**, 25323–25327.
7 K. A. Persson, B. Waldwick, P. Lazic and G. Ceder, *Phys. Rev. B*, 2012, **85**, 235438.
8 A. K. Singh, L. Zhou, A. Shinde, S. K. Suram, J. H. Montoya, D. Winston, J. M. Gregoire and K. A. Persson, *Chem. Mater.*, 2017, **29**, 10159–10167.
9 P. Munnik, P. E. de Jongh and K. P. de Jong, *Chem. Rev.*, 2015, **115**, 6687–6718.
10 Mineral-Based Synthesis of CuFe2O4 Nanoparticles via Co-Precipitation and Microwave Techniques Using Leached Copper Solutions from Mined Minerals, https://www.mdpi.com/2075-163X/15/8/819, (accessed August 30, 2025).
11 M. C. Mascolo, Y. Pei and T. A. Ring, *Materials*, 2013, **6**, 5549–5567.
12 W. S. Jr. Hummers and R. E. Offeman, *J. Am. Chem. Soc.*, 1958, **80**, 1339–1339.
13 Improved Synthesis of Graphene Oxide | ACS Nano, https://pubs.acs.org/doi/10.1021/nn1006368?utm_source=chatgpt.com, (accessed August 30, 2025).
14 F. Islam, A. Tahmasebi, B. Moghtaderi and J. Yu, *Nanomaterials*, 2022, **12**, 57.
15 Raman spectroscopy as a versatile tool for studying the properties of graphene | Nature Nanotechnology, https://www.nature.com/articles/nnano.2013.46?utm_source=chatgpt.com, (accessed August 30, 2025).

16 L. M. Malard, M. A. Pimenta, G. Dresselhaus and M. S. Dresselhaus, *Phys. Rep.*, 2009, **473**, 51–87.
17 X. Wang, L. Zhi and K. Müllen, *Nano Lett.*, 2008, **8**, 323–327.
18 K. Panchal, K. Bhakar, K. S. Sharma, D. Kumar and S. Prasad, *Appl. Spectrosc. Rev.*, 2025, **60**, 30–55.
19 Electrochemical Impedance Spectroscopy (EIS): Principles, Construction, and Biosensing Applications, https://www.mdpi.com/1424-8220/21/19/6578, (accessed August 30, 2025).
20 M. Y. Perdana, B. A. Johan, M. Abdallah, Md. E. Hossain, Md. A. Aziz, T. N. Baroud and Q. A. Drmosh, *Chem. Rec.*, 2024, **24**, e202400007.